Magnetic proximity effect in graphene coupled to a BiFeO₃ nanoplate

Yan-Fei Wu,[1,2] Hua-Ding Song,[2] Liang Zhang,[2] Xin Yang,[3] Zhaohui Ren,[3] Dameng Liu,[4] Han-Chun Wu,[5] Jansheng Wu,[1] Jin-Guang Li,[2] Zhenzhao Jia,[2] Baoming Yan,[2] Xiaosong Wu,[2,6] Chun-Gang Duan,[7] Gaorong Han,[3] Zhi-Min Liao,[2,6,*] and Dapeng Yu[1,2]

[1]*Institute for Quantum Science and Engineering and Department of Physics,*
South University of Science and Technology of China, Shenzhen 518055, China

[2]*State Key Laboratory for Mesoscopic Physics, School of Physics, Peking University, Beijing 100871, China*

[3]*State Key Laboratory of Silicon Materials, School of Materials Science and Engineering, Zhejiang University, Hangzhou 310027, China*

[4]*State Key Laboratory of Tribology, Tsinghua University, Beijing 100084, China*

[5]*School of Physics, Beijing Institute of Technology, Beijing 100081, China*

[6]*Collaborative Innovation Center of Quantum Matter, Beijing 100871, China*

[7]*Key Laboratory of Polar Materials and Devices, Ministry of Education, East China Normal University, Shanghai 200241, China*

Graphene, a very intriguing two-dimensional Dirac electronic system with high carrier mobility, is promising for spintronics. However, the long-range ferromagnetic order is always absent in pristine graphene. Here we report the fabrication and transport properties of graphene-BiFeO₃ heterostructures. It is found that the magnetic proximity effect results in a strong Zeeman splitting in graphene with the exchange field up to hundreds of tesla. The $\nu = 0$ quantum Hall state of graphene is further transformed into a ferromagnetic state or a canted antiferromagnetic state in the presence of a perpendicular magnetic field. Our findings in graphene/BiFeO₃ heterostructure are therefore promising for future spintronics.

I. INTRODUCTION

Graphene is one of the promising spintronic materials due to its high carrier mobility and long spin diffusion length [1–21]. However, the absence of notable spin-orbit coupling and ferromagnetic order in graphene limits its prospect in spintronics [1–21]. Two-dimensional (2D) materials such as graphene are predicted to experience strong exchange field in hybrid heterostructures with magnetic materials [20–22]. Because monolayer graphene has a strong hybridization with neighboring material, its electronic structure can be significantly modulated by proximity effect [22–24]. Recently, a large exchange field was observed in graphene coupled to ferromagnetic thin film [23,24]. Wang *et al.* fabricated the devices by transferring the graphene devices using polymethyl methacrylate (PMMA) onto the yttrium iron garnet (YIG) ferromagnetic thin film and observed the anomalous Hall effect in such devices [24]. Wei *et al.* fabricated the devices by depositing EuS thin film on the graphene devices and observed the Zeeman spin Hall effect [23]. Qiao *et al.* theoretically predicated that a large exchange field can also exist in graphene-BiFeO₃ (BFO) heterostructures and the large exchange splitting can be up to 70 meV (corresponding to exchange magnetic field ∼580 T) [21].

Here we report the fabrication and transport properties of graphene/BiFeO₃ heterostructures. The BFO nanoplate was stacked on the mechanically exfoliated graphene on a Si/SiO₂ substrate by a dry transfer method, in order to avoid the possible contamination from PMMA transfer technique and avoid the possible damage of graphene from the deposition of magnetic thin film. We demonstrate the large Zeeman splitting induced by exchange field in the graphene-BFO heterostructures via nonlocal measurements. Moreover, we

find that the graphene ground state ($\nu = 0$ quantum Hall state) in the graphene-BFO heterostructures is dramatically changed as applying an external magnetic field, which can be interpreted within the frame of quantum Hall ferromagnetism (QHFM).

II. METHODS

Material preparation. BFO bulks were grown by hydrothermal method [25], and then the bulks were smashed into nanoplates by ultrasonic wave. Graphene samples were acquired by a micromechanical cleavage method on Si wafers with a 285 nm SiO₂ coating layer. The TEM characterizations were performed in a FEI Tecnai F20 transmission electron microscopy.

Fabrication of the devices. The fabrication details about the stacking of BFO nanoplates on monolayer graphene on a Si substrate with a 285 nm SiO₂ layer were described in Fig. 1. The BFO nanoplates were transferred onto graphene by a micromanipulator similar with other works [26]. Pd/Au electrodes (5 nm/80 nm) were fabricated after a series of processes containing electron beam lithography (EBL), metal deposition techniques, and lift-off.

Transport measurements. The magnetotransport measurements were performed in a modified Oxford dilution refrigerator which can also provide 14 T magnetic field and temperature down to 95 mK. The nonlocal and four-terminal electrical measurements were carried out through lock-in amplifiers by applying 0.1 μA current with a locked frequency of 17.7 Hz.

III. RESULTS AND DISCUSSION

The interface of the graphene-BFO hybrid devices is illustrated in Fig. 2(a). The BFO nanoplates are single crystals. The measured lattice spacing of $d = 0.402$ nm matches the spacing of the (012) lattice plane of a rhombohedral phase BiFeO₃

*liaozm@pku.edu.cn
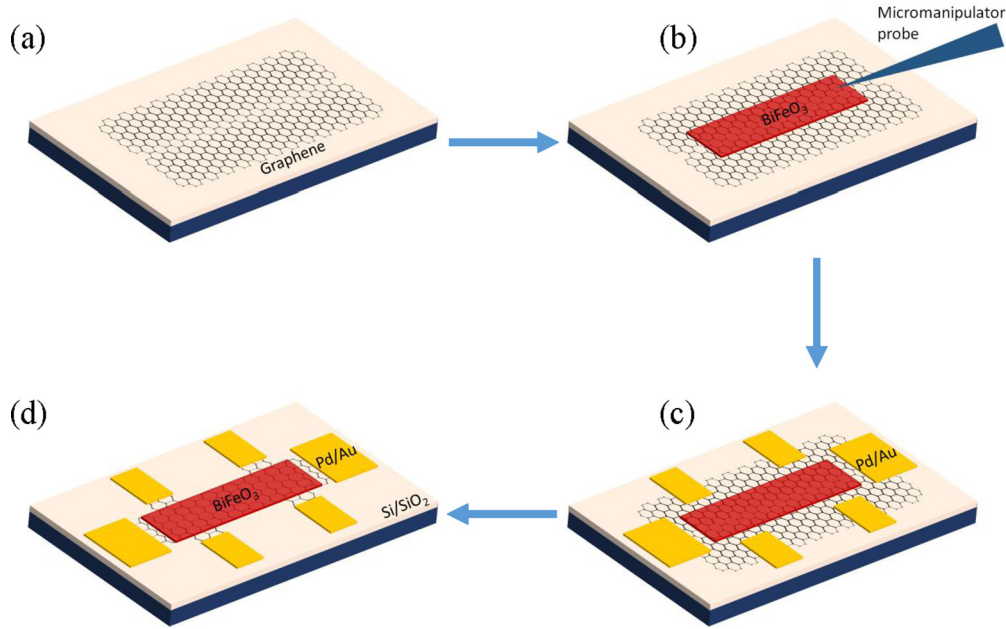
FIG. 1. Fabrication of BiFeO$_3$-graphene hybrid devices. The BiFeO$_3$-graphene hybrid transistors were fabricated as following processes. (a) Monolayer graphene sheets were exfoliated by scotch tape method on Si substrate with a 285 nm SiO$_2$ layer. (b) BiFeO$_3$ nanoplates grown by hydrothermal method were transferred onto graphene by a micromanipulator. (**c**) Electron beam lithography (EBL) and electron beam evaporation techniques were used to fabricate Pd/Au (5 nm/80 nm) electrodes. (d) Hall-bar structure was shaped by oxygen plasma etching after another round of EBL.

crystal, as shown by the transmission electron microscopy (TEM) image in Fig. 2(b). The BFO surface contacted to graphene is the (100)$_c$ pseudocubic crystal plane. It has been reported that the BFO single crystal thin film exhibits weak ferromagnetism as a result of the canted spin structure [27,28]. Although the BFO (100) plane facing the graphene is not the preferred (111) plane where the Fe ions are aligned

ferromagnetically [21], the substantial exchange interaction between graphene π orbitals and the 3d orbitals of the Fe layer in BFO may still have a notable effect. In our experiments, an external magnetic field was further applied to produce the net magnetic moments on the (100) plane.

The schematic diagram of a typical BFO-graphene device with Hall bar configuration is shown in Fig. 2(c). The channel length of the Hall bar between the two-voltage leads is $L = 4\,\mu$m and the width is $W = 3.24\,\mu$m. The mobility of the hybrid device is $\sim$10^4 cm^2/V s calculated from the transfer curve shown in Fig. 2(d).

For the graphene system with large exchange field, strong Zeeman splitting can be expected. A band structure diagram for spin-polarized graphene with strong Zeeman splitting is illustrated in Fig. 3(a). The spin-up and spin-down subbands are separated by the exchange field induced Zeeman splitting [20,21]. The Dirac cones of corresponding spin are lifted towards opposite directions, and a simultaneous concentration of spin-up holes and spin-down electrons is produced as the Fermi level lies between the Dirac points [29–32]. The Zeeman splitting can cause an obvious nonlocal signal, which is sharply enhanced near the Dirac point [29–32]. As shown in Fig. 3(b), two nonlocal measurement configurations are used to probe the nonlocal current. Figures 3(c) and 3(d) show the back-gate voltage (V_g) versus nonlocal resistivity (R_{nl}) under 0 and 0.5 T perpendicular magnetic field, respectively. For $B_\perp = 0$, there are almost identical nonlocal signals for the two measurement configurations [Fig. 3(c)]. The Ohmic contribution to the nonlocal signal
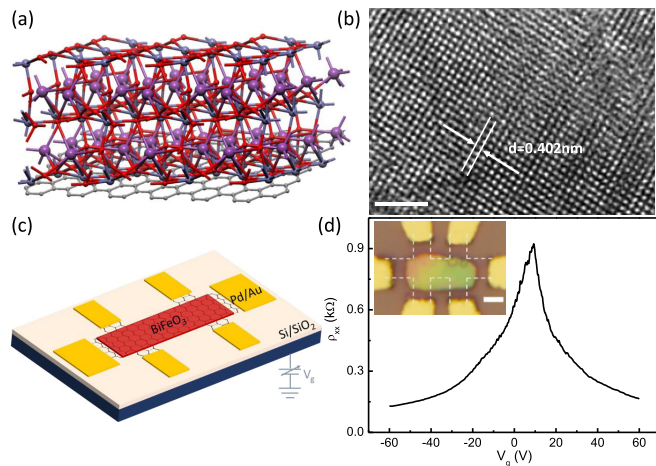
FIG. 2. Characterization of BiFeO$_3$/graphene heterostructure. (a) Diagram of the crystal structure of BiFeO$_3$/graphene hybrid heterostructure. Red atoms: oxygen; dark gray atoms: iron; purple atoms: bismuth; light gray atoms: carbon. (b) High resolution TEM image of a typical BiFeO$_3$ nanoplate. Scale bar: 2 nm. (c) Diagram for the device. (d) Back-gate voltage dependence of resistivity of the BFO/graphene hybrid device. Inset: Optical image of a typical BFO/graphene hybrid transistor. The scale bar is 2 μm.

$$R_{\text{nl}}^O \sim \frac{1}{\pi}\rho_{xx}\left\{\ln\left[\cosh\left(\frac{\pi l}{w}\right)+1\right]-\ln\left[\cosh\left(\frac{\pi l}{w}\right)-1\right]\right\},$$
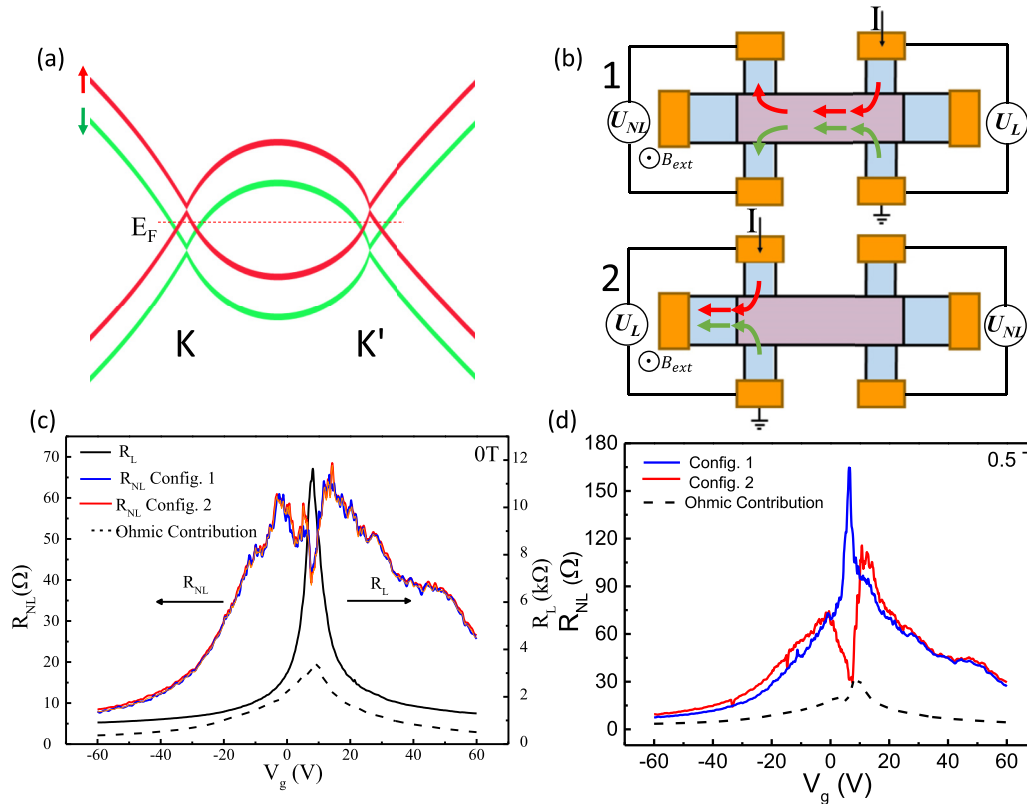
FIG. 3. Low field nonlocal measurement results. (a) Diagram for graphene band structure containing Zeeman splitting. Red (green) arrow denotes spin-up (spin-down). (b) Schematics for measurement configurations 1 and 2. (c) and (d) Nonlocal resistivity measured under external magnetic field of 0 and 0.5 T, respectively, with configurations 1 (blue) and 2 (red).

based on the van der Pauw formalism [29–32], is displayed by a dashed line, indicating the nonlocal signal is evidently enhanced compared to the classical Ohmic leakage. We propose that spin polarization induced by the exchange field may give rise to spin Hall effect leading to the nonlocal signals under $B_\perp = 0$ T [1,32].

For $B_\perp = 0.5$ T, the nonlocal resistance ($R_{nl} = V_{nl}/I$) near the Dirac point has opposite behavior for the two measurement configurations, affirming significant influence of Lorentz force on the nonlocal transport. The R_{nl} detected by configuration 2 is quite close to the Ohmic contribution at the Dirac point. However, the nonlocal resistance of configuration 1 is much stronger than the Ohmic contribution. According to the fact that electrons and holes move oppositely in the applied source current, the Lorentz force drives the two types of carriers along the same direction in the Hall bar channel. For configuration 1, the electrons and holes diffuse to the remote area and then are separated oppositely due to the Lorenz force by the external magnetic field, resulting in the voltage drop between the two voltage probes and the nonlocal resistance [29–32]. For configuration 2, the electrons and holes near the Dirac point cannot reach the graphene area with the nonlocal probes, and the nonlocal signals will be sharply suppressed. The large Zeeman splitting in graphene is further confirmed by the nonlocal measurement results while changing the polarity of the magnetic field (Fig. 4). As shown in Fig. 4, the V_g dependence of the nonlocal resistance measured with negative magnetic field and measurement configuration 1 is very

similar with that measured with positive magnetic field and measurement configuration 2. These results are well consistent with the spin polarization origin of the nonlocal signal, because the carriers move in the opposite direction by changing the polarity of the magnetic field.

To further reveal the magnetotransport properties, the back-gate modulation of longitudinal resistivity (ρ_{xx}) was measured by the four-terminal method using a Hall bar configuration with $B_\perp$ up to 14 T. We use $V_g^{\pm 1}$ to label the gate voltage where Fermi level E_F locates at the $N = \pm 1$ Landau level center. When E_F lies at the ± 1st LL center, the carriers injected into graphene by gate voltage can be described as $4e^2 B_\perp / h$, considering spin and valley degree in graphene. By the capacitance model we have $V_g^1 = V_D + 4e^2 B_\perp / h C_{\mathrm{SiO_2}}$. As shown in Fig. 5, the Dirac point position (V_D) ~ 6.2 V is derived from the dependence between $V_g^{\pm 1}$ and $B_\perp$. Accordingly, the filling factor ν can be obtained by

$$\nu = nh/eB_\perp = \frac{(V_g - V_D)C_{\mathrm{SiO_2}}}{e} \frac{h}{eB_\perp}.$$

The ρ_{xx} as a function of ν at different external magnetic fields is displayed in Fig. 6(a).

As shown in Fig. 6(a), an anomalous resistivity dip exists inside the $N = 0$ Landau level (LL) (near $\nu = 0$), enclosed by two resistivity peaks centered around $\nu = \pm 1$. The anomalous resistivity dip activated by low magnetic field is reproducible in other devices. Under low magnetic field ($B_\perp = 0 - 2$ T),
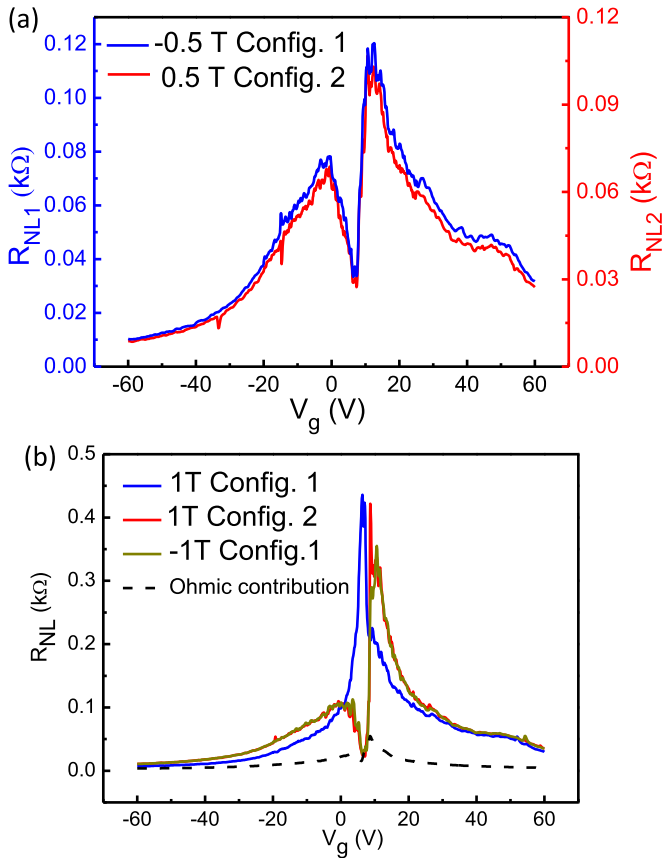
FIG. 4. Nonlocal measurement results with both positive and negative magnetic fields. (a) The nonlocal resistance measured with -0.5 T and measurement configuration 1 (blue curve), and with 0.5 T and measurement configuration 2 (red curve). It is clear that the R_{nl}-V_g curves exhibit similar relationship for the two measurement configurations with opposite polarity of the magnetic field. (b) The nonlocal resistance measured with 1 T and measurement configuration 1 (blue curve), with 1 T and measurement configuration 2 (red curve), and with -1 T and measurement configuration 1 (brown curve).

a negative magnetoresistance behavior is observed at $\nu = 0$ with decreasing $\rho_{xx,D}$ (ρ_{xx} at $\nu = 0$), and $\rho_{xx,D}$ maintains a quite low value (< 1 kΩ) for $B_\perp < 10$ T [Fig. 6(b)]. After $B_\perp$ exceeds 10 T, a dramatic increase of $\rho_{xx,D}$ occurs, it seems that an energy gap is opened inside the $N = 0$ LL. These features are totally different from conventional graphene samples. Nevertheless, the resistivity peaks caused by the population of $N = \pm 1$ Landau level (around $\nu = \pm 4$), and the zero resistivity originating from quantum Hall edge states (around $\nu = \pm 2, \pm 6$) are clearly displayed as well, showing typical quantum Hall effect behaviors of graphene. The magnetic proximity effect mainly affects the $\nu = 0$ states. Correspondingly, the Hall conductivity under $B_\perp = 14$ T exhibits typical half-integer Hall plateaus. The sharply divergence of $\sigma_{xy} = \rho_{xx}/\rho_{xx}^2 + \rho_{xy}^2$ near $\nu = 0$ is caused by the anomalous resistivity dip [Fig. 6(c)]. These features indicate that the nonzero energy modes remain typical graphene Landau level structures. Therefore, the intriguing behavior near $\nu = 0$ is strongly related to the novel electronic structure of graphene ground state.
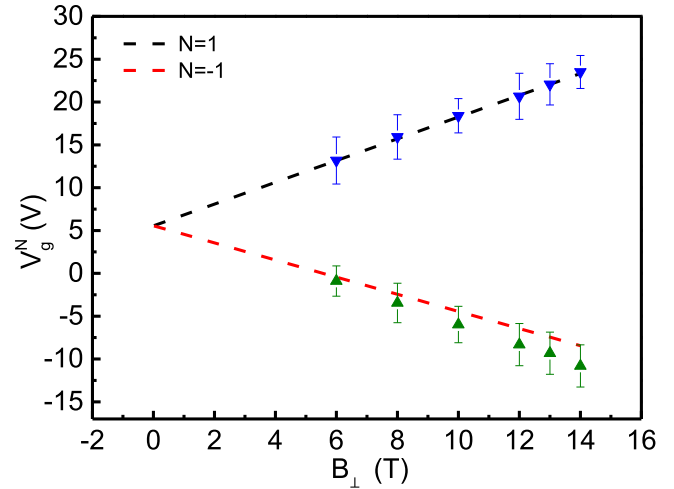
FIG. 5. The theoretical predictions (dashed lines) and experimental results (blue triangle: $N = +1$; green triangle: $N = -1$) of $N = \pm 1$ LL positions are compared.

The anomalous transport properties inside the $N = 0$ LL can be well described by the framework of QHFM theory [33–37]. The graphene $N = 0$ LL have three possible phases: (1) The valley-polarized antiferromagnetic (AFM) phase, where the ground state is completely insulating with gapped edge states ($\Delta_{edge} = \Delta_{bulk}$) [Fig. 6(d)]. (2) The canted antiferromagnetic (CAF) phase, an intermediate phase ($\Delta_{edge} < \Delta_{bulk}$) smoothly converts between the above two phases [Fig. 6(e)]. (3) The spin-polarized ferromagnetic (FM) phase, where gapless counter-circulating edge states with opposite spin projections exist inside the $N = 0$ LL ($\Delta_{edge} = 0$) [Fig. 6(f)]. The competition between valley isospin anisotropy energy ($u_\perp$) and Zeeman splitting energy (E_Z) determines the ground state phases of the system [33–37]: $E_Z \geqslant 2|u_\perp|$ for FM phase, and $0 < E_Z < 2|u_\perp|$ for CAF phase. The physical origin of $u_\perp$ can be traced to the strong Coulomb interactions within graphene $N = 0$ LL. Since $u_\perp \sim \frac{e^2 a}{l_B^2} = \frac{e^3 a}{c} B_\perp$, where $l_B = \sqrt{\frac{c}{e B_\perp}}$ (taking $\hbar = 1$ here) is the magnetic length and a is a lattice constant scale quantity, it is clear that the $u_\perp$ only relies on $B_\perp$ [33–37]. The E_Z, representing the magnitude of spin polarization, include the contributions from the external magnetic field $B_\perp$ and the spin splitting caused by exchange field. The exchange field has almost no influence on $u_\perp$, because it cannot affect the orbital energy or the many-body correlations within LLs [33–37].

Now we can consider the exchange field as an analogical field B_{exc} which is nearly irrelevant to the real external field $B_\perp$, then the total Zeeman splitting energy is $E_Z = \mu_B(B_{exc} + B_\perp)$. We have already verified that exchange field is introduced into graphene by the proximity effect of BFO, thus for $B_\perp = 0$ we have $E_{Z0} = \mu_B B_{exc} > u_\perp = 0$. By adjusting $B_\perp$, the graphene ground state can preserve FM phase under moderate external field ($2|u_\perp| \leqslant E_Z$), then transform to CAF phase under large enough external field ($2|u_\perp| > E_Z$). This scenario fits our results in Fig. 6(a). For $B_\perp \leqslant 10$ T, the edge states of FM phase induces low $\rho_{xx,D}$, and for $B_\perp \geqslant 10$ T, the gap opening of CAF phase creates the rise of $\rho_{xx,D}$ and an anomalous resistivity peak emerge near $\nu = 0$.
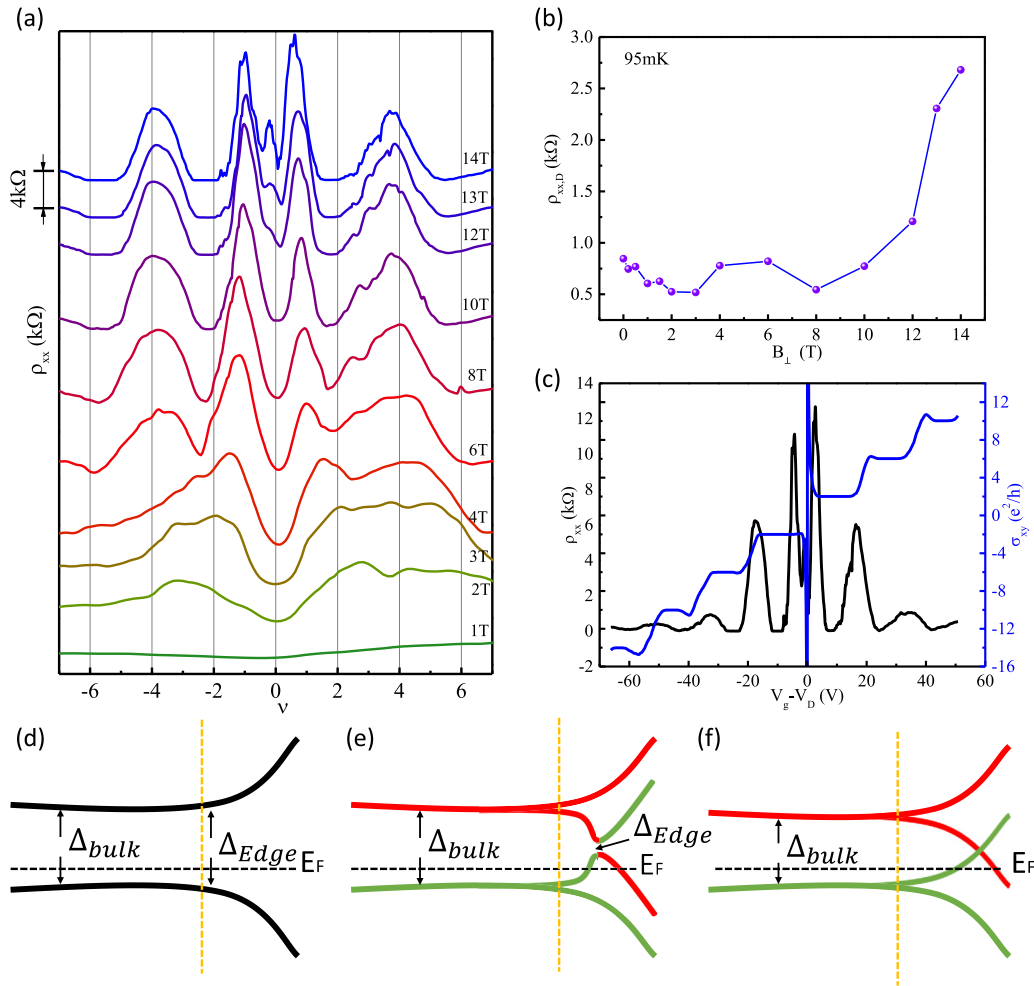
FIG. 6. Four-terminal measurement results. (a) Longitudinal resistivity measured by four-terminal configuration under external field from 0.5 to 14 T. For clarity of linear fitting of the LL, the curves are shifted in direct proportion to the applied magnetic field. (b) $\rho_{xx} \sim B_\perp$ evolution at $\nu = 0$. (c) Transverse conductivity σ_{xy} and longitudinal resistivity ρ_{xx} measured under 14 T. (d)–(f) Illustrations of the antiferromagnetic, canted antiferromagnetic, and ferromagnetic phases with spin-momentum locked helical edge states.

The transformation between FM and CAF phases is further confirmed by nonlocal magnetotransport measurements. Obvious nonlocal resistance is observed at the Dirac point under large external magnetic field [Fig. 7(a)]. It is worth to note that a sudden decrease of R_{nl} near the Dirac point was clearly observed under $B_\perp = 12$ and 13 T [Fig. 7(a)], consistent with the emergence of gapped edge states. It is also found that the R_{nl} peak tends to be suppressed from 8 to 13 T [Fig. 7(b)]. As the system transforms from the FM to the CAF phase with the opening of an edge state gap [33–37], the edge states are absent within the gap, resulting in the decrease of the nonlocal signal. The drop of R_{nl} near the Dirac point under $B_\perp = 13$ T is further confirmed to occur inside the $N = 0$ LL by the distinct QH plateaus of the two-terminal resistance R_L [Fig. 7(c)]. The R_L at the Dirac point increases dramatically with $B_\perp > 10$ T [Fig. 7(d)], which also results from the edge state gap opening.

The experimental results show that the FM to CAF phase transformation occurs at $B_\perp \sim 10$ T. Because the dipolar magnetic field of antiferromagnetic insulator BFO is very

weak, the contribution of BFO in valley isospin anisotropy energy $u_\perp$ and Zeeman splitting E_Z can be neglected [20,21]. Therefore, the $u_\perp \sim \frac{e^3 a}{c} B_\perp$ (taking $\hbar = 1$) can be estimated as $\sim (1$–$10)B_\perp / K$ according to the lower and upper limits of the lattice spatial parameter a [33–37]. Considering the existence of exchange field, the Zeeman splitting in our system is a sum of intrinsic and external contributions: $E_Z = \mu_B(B_\perp + B_{exc})$. At the critical point it should be $E_Z = 2|u_\perp|$ [30–32]. Giving $B_\perp = 10$ T, the lower and upper limits of B_{exc} are estimated to be 19.8–287.9 T. Such a substantial exchange field is actually guaranteed by the strong exchange interaction (1 eV) of the Fe 3d states [27]. A recent work reported the exchange field in graphene coupled to EuS is >14 T [23]. Although it seems surprising that BFO induces a larger exchange field, this result is reasonable because the 4d states of Eu provide a weaker exchange interaction ($\sim$0.77 eV) [38]. The exchange splitting in graphene/EuO system is predicted as 36 meV [38], obviously smaller than the 70 meV in graphene/BFO system [21].
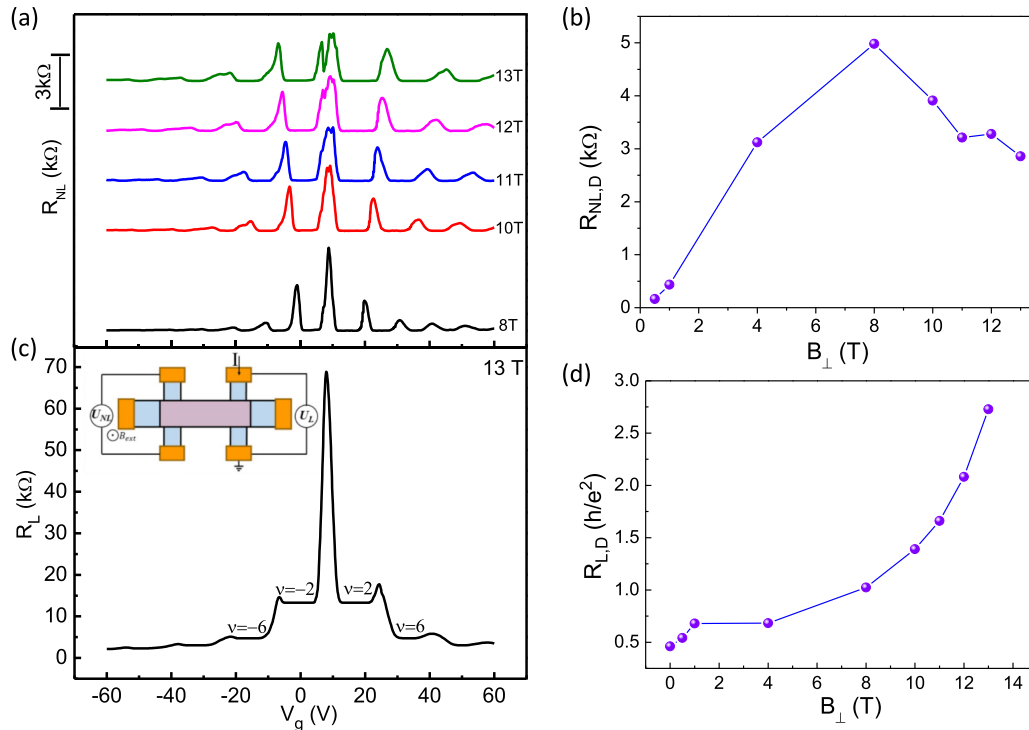
FIG. 7. Magnetotransport nonlocal measurement results. (a) Nonlocal resistance $R_{\rm nl}$ measured under 8–13 T perpendicular external field. The reduction of $R_{\rm nl}$ emerges under 12/13 T is further evidence for FM-CAF phase transition in LL ground state. (Inset: Nonlocal measurement configuration.) (b) The $R_{\rm nl}$ peak value [highest points of the curves in panel (a)] also decreases as the field increases from 8 to 13 T. (c) Two-terminal resistance R_L obtained under $B_\perp = 13$ T. Part of QHE plateaus are defined as $\nu = \pm 2$ ($\frac{h}{2e^2} \sim 12.9$ kΩ) and $\nu = \pm 6$ ($\frac{h}{6e^2} \sim 4.3$ kΩ). (d) Evolution of $R_{L,D}$ at the Dirac point (the highest point) with increasing external field. It is very obvious that $R_{L,D}$ rapidly rises after $B_\perp = 10$ T, indicating the gap opening.

IV. CONCLUSIONS

In conclusion, we have demonstrated the transport properties of BiFeO$_3$/graphene heterostructures. Large nonlocal signal under low external field, and anomalous low resistivity transport near the Dirac point, is attributed to large Zeeman splitting caused by exchange field. With increasing external perpendicular magnetic field, the $N = 0$ Landau level of graphene transforms from a ferromagnetic state to a canted antiferromagnetic state, a substantial exchange field up to 287.9 T is revealed by analyzing the critical point. We wish our findings can inspire further explorations on graphene/BFO hybrid system, for detailed explanations of these novel phenomena. Our work should shed light on the exploration on graphene-based proximity effect, and investigations of high-efficiency electronics and topological quantum spintronic devices.

[1] D. Xiao, M.-C. Chang, and Q. Niu, Berry phase effects on electronic properties, Rev. Mod. Phys. **82**, 1959 (2010).

[2] M. Z. Hasan and C. L. Kane, Colloquium: Topological insulators, Rev. Mod. Phys. **82**, 3045 (2010).

[3] C. L. Kane and E. J. Mele, Z$_2$ Topological Order and the Quantum Spin Hall Effect, Phys. Rev. Lett. **95**, 146802 (2005).

[4] M. Büttiker, Absence of backscattering in the quantum Hall effect in multiprobe conductors, Phys. Rev. B **38**, 9375 (1988).

[5] D. C. Tsui, H. L. Stormer, and A. C. Gossard, Two-Dimensional Magnetotransport in the Extreme Quantum Limit, Phys. Rev. Lett. **48**, 1559 (1982).

[6] A. H. Castro Neto, N. M. R. Peres, K. S. Novoselov, and A. K. Geim, The electronic properties of graphene, Rev. Mod. Phys. **81**, 109 (2009).

[7] S. Das Sarma, S. Adam, E. H. Hwang, and E. Rossi, Electronic transport in two-dimensional graphene, Rev. Mod. Phys. **83**, 407 (2011).

[8] K. S. Novoselov, A. K. Geim, S. V. Morozov, D. Jiang, M. I. Katsnelson, I. V. Grigorieva, S. V. Dubonos, and A. A. Firsov, Two-dimensional gas of massless Dirac fermions in graphene, Nature (London) **438**, 197 (2005).

[9] Y. Zhang, Y. W. Tan, H. L. Stormer, and P. Kim, Experimental observation of the quantum Hall effect and Berry's phase in graphene, Nature (London) **438**, 201 (2005).

[10] A. Roth, C. Brüne, H. Buhmann, L. W. Molenkamp, J. Maciejko, X.-L. Qi, and S.-C. Zhang, Nonlocal transport in the quantum spin Hall state, Science **325**, 294 (2009).

[11] C. L. Kane and E. J. Mele, Quantum Spin Hall Effect in Graphene, Phys. Rev. Lett. **95**, 226801 (2005).

[12] D. Hsieh, D. Qian, L. Wray, Y. Xia, Y. S. Hor, R. J. Cava, and M. Z. Hasan, A topological Dirac insulator in a quantum spin Hall phase, Nature (London) **452**, 970 (2008).

[13] B. A. Bernevig, T. L. Hughes, and S.-C. Zhang, Quantum spin Hall effect and topological phase transition in HgTe quantum wells, Science **314**, 1757 (2006).

[14] F. D. Haldane, Model for a Quantum Hall Effect without Landau Levels: Condensed-Matter Realization of the "Parity Anomaly", Phys. Rev. Lett. **61**, 2015 (1988).

[15] C. Z. Chang, J. Zhang, X. Feng, J. Shen, Z. Zhang, M. Guo, K. Li, Y. Ou, P. Wei, L. L. Wang, Z. Q. Ji, Y. Feng, S. Ji, X. Chen, J. Jia, X. Dai, Z. Fang, S. C. Zhang, K. He, Y. Wang, L. Lu, X. C. Ma, and Q. K. Xue, Experimental observation of the quantum anomalous Hall effect in a magnetic topological insulator, Science **340**, 167 (2013).

[16] C. Z. Chang, W. Zhao, D. Y. Kim, H. Zhang, B. A. Assaf, D. Heiman, S. C. Zhang, C. Liu, M. H. Chan, and J. S. Moodera, High-precision realization of robust quantum anomalous Hall state in a hard ferromagnetic topological insulator, Nat. Mater. **14**, 473 (2015).

[17] R. Yu, W. Zhang, H. J. Zhang, S. C. Zhang, X. Dai, and Z. Fang, Quantized anomalous Hall effect in magnetic topological insulators, Science **329**, 61 (2010).

[18] K. S. Novoselov, A. K. Geim, S. Morozov, D. Jiang, Y. Zhang, S. Dubonos, I. Grigorieva, and A. Firsov, Electric field effect in atomically thin carbon films, Science **306**, 666 (2004).

[19] A. K. Geim and K. S. Novoselov, The rise of graphene, Nat. Mater. **6**, 183 (2007).

[20] Z. Qiao, S. A. Yang, W. Feng, W.-K. Tse, J. Ding, Y. Yao, J. Wang, and Q. Niu, Quantum anomalous Hall effect in graphene from Rashba and exchange effects, Phys. Rev. B **82**, 161414 (2010).

[21] Z. Qiao, W. Ren, H. Chen, L. Bellaiche, Z. Zhang, A. H. MacDonald, and Q. Niu, Quantum Anomalous Hall Effect in Graphene Proximity Coupled to an Antiferromagnetic Insulator, Phys. Rev. Lett. **112**, 116404 (2014).

[22] H. Haugen, D. Huertas-Hernando, and A. Brataas, Spin transport in proximity-induced ferromagnetic graphene, Phys. Rev. B **77**, 115406 (2008).

[23] P. Wei, S. Lee, F. Lemaitre, L. Pinel, D. Cutaia, W. Cha, F. Katmis, Y. Zhu, D. Heiman, J. Hone, J. S. Moodera, and C. T. Chen, Strong interfacial exchange field in the graphene/EuS heterostructure, Nat. Mater. **15**, 711 (2016).

[24] Z. Wang, C. Tang, R. Sachs, Y. Barlas, and J. Shi, Proximity-Induced Ferromagnetism in Graphene Revealed by the Anomalous Hall Effect, Phys. Rev. Lett. **114**, 016603 (2015).

[25] X. Yang, G. Xu, Z. Ren, X. Wei, C. Chao, S. Gong, G. Shen, and G. Han, The hydrothermal synthesis and formation mechanism of single-crystalline perovskite BiFeO$_3$ microplates with dominant (012) facets, Cryst. Eng. Commun. **16**, 4176 (2014).

[26] L. Zhang, Y. Yan, H.-C. Wu, D. P. Yu, and Z.-M. Liao, Gate-tunable tunneling resistance in graphene/topological insulator vertical junctions, ACS Nano **10**, 3816 (2016).

[27] C. Ederer and N. A. Spaldin, Weak ferromagnetism and magnetoelectric coupling in bismuth ferrite, Phys. Rev. B **71**, 060401(R) (2005).

[28] J. Wang, J. Neaton, H. Zheng, V. Nagarajan, S. Ogale, B. Liu, D. Viehland, V. Vaithyanathan, D. Schlom, and U. Waghmare, Epitaxial BiFeO$_3$ multiferroic thin film heterostructures, Science **299**, 1719 (2003).

[29] D. A. Abanin, S. V. Morozov, L. A. Ponomarenko, R. V. Gorbachev, A. S. Mayorov, M. I. Katsnelson, K. Watanabe, T. Taniguchi, K. S. Novoselov, L. S. Levitov, and A. K. Geim, Giant nonlocality near the Dirac point in graphene, Science **332**, 328 (2011).

[30] D. A. Abanin, R. V. Gorbachev, K. S. Novoselov, A. K. Geim, and L. S. Levitov, Giant Spin-Hall Effect Induced by the Zeeman Interaction in Graphene, Phys. Rev. Lett. **107**, 096601 (2011).

[31] D. A. Abanin, A. V. Shytov, L. S. Levitov, and B. I. Halperin, Nonlocal charge transport mediated by spin diffusion in the spin Hall effect regime, Phys. Rev. B **79**, 035304 (2009).

[32] J. Renard, M. Studer, and J. A. Folk, Origins of Nonlocality near the Neutrality Point in Graphene, Phys. Rev. Lett. **112**, 116601 (2014).

[33] M. Kharitonov, Canted Antiferromagnetic Phase of the $\nu = 0$ Quantum Hall State in Bilayer Graphene, Phys. Rev. Lett. **109**, 046803 (2012).

[34] M. Kharitonov, Phase diagram for the $\nu = 0$ quantum Hall state in monolayer graphene, Phys. Rev. B **85**, 155439 (2012).

[35] M. Kharitonov, Edge excitations of the canted antiferromagnetic phase of the $\nu = 0$ quantum Hall state in graphene: A simplified analysis, Phys. Rev. B **86**, 075450 (2012).

[36] K. Nomura and A. H. MacDonald, Quantum Hall Ferromagnetism in Graphene, Phys. Rev. Lett. **96**, 256602 (2006).

[37] A. F. Young, J. D. Sanchez-Yamagishi, B. Hunt, S. H. Choi, K. Watanabe, T. Taniguchi, R. C. Ashoori, and P. Jarillo-Herrero, Tunable symmetry breaking and helical edge transport in a graphene quantum spin Hall state, Nature (London) **505**, 528 (2014).

[38] H. X. Yang, A. Hallal, D. Terrade, X. Waintal, S. Roche, and M. Chshiev, Proximity Effects Induced in Graphene by Magnetic Insulators: First-Principles Calculations on Spin Filtering and Exchange-Splitting Gaps, Phys. Rev. Lett. **110**, 046603 (2013).